Patterns in thin vibrated granular layers: Interfaces, hexagons, and superoscillons

D. Blair, I. S. Aranson, G. W. Crabtree, and V. Vinokur
Argonne National Laboratory, 9700 South Cass Avenue, Argonne, Illinois 60439

L. S. Tsimring
Institute for Nonlinear Science, University of California, San Diego, La Jolla, California 92093-0402

C. Josserand
James Frank Institute, University of Chicago, 5640 S. Ellis Avenue, Chicago, Illinois 60637

(Received 6 October 1999)

A theoretical and experimental study of patterns in vibrated granular layers is presented. An order parameter model based on the parametric Ginzburg-Landau equation is used to describe strongly nonlinear excitations including hexagons, interfaces between flat antiphase domains, and new localized objects, *superoscillons*. The experiments confirm the existence of superoscillons and bound states of superoscillons and interfaces. On the basis of the order parameter model we predict analytically and confirm experimentally that additional subharmonic driving results in the controlled motion of interfaces.

PACS number(s): 47.54.+r, 47.35.+i, 45.05.+x, 83.70.Fn

INTRODUCTION

The collective dynamics of granular materials is a subject of current interest [1–5]. The intrinsic dissipative nature of the interactions between the constituent macroscopic particles gives rise to several basic properties specific to granular substances which set granular matter apart from conventional gaseous, liquid, or solid states.

Driven granular systems manifest collective fluidlike behavior: convection, surface waves, and pattern formation (see, e.g., Ref. [1]). One of the most fascinating examples of collective dynamics in these materials is the appearance of long-range coherent patterns and localized excitations in vertically vibrated thin granular layers [2–8]. The particular pattern is determined by the interplay between driving frequency f and acceleration of the container $\Gamma = 4\pi^2 \mathcal{A} f^2/g$ ($\mathcal{A}$ is the amplitude of oscillations, g is the acceleration due to gravity) [2,3].

Patterns appear at $\Gamma \approx 2.4$ almost independently of the driving frequency f. At small frequencies $f < f^*$ [3,4] the transition is subcritical (hysteretic), leading to the formation of squares. In the hysteretic region, localized excitations such as individual *oscillons* as well as bound states of oscillons appear as Γ is decreased. For higher frequencies $f > f^*$ the pattern becomes stripes, and at frequencies slightly higher than f^* the transition becomes supercritical. Both squares and stripes, as well as oscillons, oscillate at half of the driving frequency $f/2$. At higher acceleration ($\Gamma > 4$), stripes and squares become unstable, and hexagons appear instead. When the driving acceleration is increased further $\Gamma \approx 4.5$ hexagons are converted into a domainlike structure of flat layers oscillating with frequency $f/2$ with opposite phases. Depending on parameters, interfaces which separate flat domains are either smooth or ''decorated'' by periodic undulations. For $\Gamma > 5.7$ various quarter-harmonic patterns emerge.

Pattern formation in thin layers of granular material were studied theoretically by several groups. Direct molecular dynamics simulations [9,10] (see also Ref. [11]) reproduced a majority of patterns observed in experiments, and many features of the bifurcation diagram. Until now these studies have not yielded superoscillons and interfaces. Hydrodynamic and phenomenological models [12,13] reproduced certain experimental features; however, neither of these offered a complete description of the rich variety of the observed phenomena. In Refs. [14,15] we introduced the order parameter characterizing the complex amplitude of subharmonic oscillations. The equations of motion following from the symmetry arguments and mass conservation reproduced the essential phenomenology of patterns near the threshold of the primary bifurcation: stripes, squares, and, localized objects, oscillons.

In this paper we describe high-acceleration patterns on the basis of the same order parameter model and compare it with experimental observations. Our preliminary results were published earlier in Refs. [5,15,16]. Here we show that at large amplitude of driving both hexagons and interfaces emerge. We find a morphological instability leading to the formation of ''decorated'' interfaces. We study the motion of the interface under the influence of a small subharmonic component in the driving acceleration. We also find a new localized structure, a ''superoscillon,'' which exists for high-acceleration values. We discuss possible mechanisms of saturation of the interface instability. Our experimental results demonstrate the existence of superoscillons and bound states of superoscillons and interfaces. They also confirm our theoretical predictions for the external control of interface motion.

The structure of the paper is as follows. In Sec. I we introduce our phenomenological order-parameter model. In Sec. II we develop the weakly nonlinear theory for the flat period-doubled state of the vibrated layer. In Sec. III we analyze the interface solution, and study its stability with respect to transverse perturbations. In Sec. IV we discuss

new localized solutions. In Sec. V we present the combined theoretical phase diagram of the model. In Sec. VI we demonstrate that in a certain limit our model can be reduced to the real Swift-Hohenberg equation. This equation also possesses a similar variety of patterns including stripes, hexagons, stable and unstable interface solutions, and localized solutions. In Sec. VII we demonstrate that additional subharmonic driving results in drift of the interface with the velocity determined by the amplitude of the driving and the direction determined by the relative phase. In Sec. VIII we present our experimental results. This includes a phase diagram and the effect of additional subharmonic driving. Section IX summarizes our conclusions.

I. PARAMETRIC GINZBURG-LANDAU EQUATION

The essence of the model [14,15] is the order-parameter equation for the complex amplitude ψ of parametric layer oscillations $h=\psi\exp(i\pi ft)+$c.c. at the frequency $f/2$ coupled with the equation for the thickness of the layer ρ averaged over the period of vibrations:

$$\partial_t\psi=\gamma\psi^*-(1-i\omega)\psi+(1+ib)\nabla^2\psi-|\psi|^2\psi-\rho\psi, \quad (1)$$

$$\partial_t\rho=\zeta\nabla\cdot(\rho\nabla|\psi|^2)+\beta\nabla^2\rho. \quad (2)$$

Here γ is the normalized amplitude of forcing at the frequency f. Linear terms in Eq. (1) can be obtained from the complex growth rate for infinitesimal periodic layer perturbations $h\sim\exp[\Lambda(k)t+ikx]$. Expanding $\Lambda(k)$ for small k, and keeping only two leading terms in the expansion $\Lambda(k)=-\Lambda_0-\Lambda_1k^2$, we obtain the linear terms in Eq. (1), where $b=\mathrm{Im}\,\Lambda_1/\mathrm{Re}\,\Lambda_1$ characterizes the ratio of dispersion to diffusion and parameter $\omega=(\Omega_0-\pi f)/\mathrm{Re}\,\Lambda_0$, $\Omega_0=-\mathrm{Im}\,\Lambda_0$, characterizes the frequency of the driving. In Eq. (2), ζ and β are transport coefficients for ρ. The slowly varying thickness of the layer ρ controls the dissipation rate [the last term in Eq. (1)]. The second equation (2) describes the redistribution of the averaged thickness due to the diffusive flux $\propto-\nabla\rho$, and an additional flux $\propto-\rho\nabla|\psi|^2$ caused by the spatially nonuniform vibrations of the granular material. This coupled model was used in Refs. [14,15] to describe pattern selection near the threshold of the primary bifurcation. It was shown that at small $\zeta\rho_0\beta^{-1}$ (which corresponds to low frequencies and thick layers) the primary bifurcation is subcritical, and leads to the emergence of square patterns. For higher frequencies and/or thinner layers, the transition is supercritical and leads to roll patterns. At intermediate frequencies ($f\approx f^*$), the stable localized solutions of Eqs. (1) and (2), corresponding to isolated *oscillons* and a variety of bound states, were found to be in agreement with experiment.

In this paper we focus on high-acceleration patterns at high frequencies. In Ref. [14] it was indicated that the density transport coefficient β is proportional to the energy of the plate vibration ($\propto\mathcal{A}^2f^2$), where $\mathcal{A}$ is the amplitude of the vibration, therefore, it should increase with the driving frequency f. As a result, for high frequencies the coupling between ρ and ψ becomes less relevant, and one can assume $\rho=$const and exclude it from Eq. (1) by rescaling. Then the model can be reduced to a single order-parameter equation

$$\partial_t\psi=\gamma\psi^*-(1-i\omega)\psi+(1+ib)\nabla^2\psi-|\psi|^2\psi. \quad (3)$$

Equation (3) also describes the evolution of the order parameter for the parametric instability in vertically oscillating fluid layers (see Refs. [17,18]).

It is convenient to shift the phase of the complex order parameter via $\tilde{\psi}=\psi\exp(i\phi)$ with $\sin 2\phi=\omega/\gamma$. The equations for the real and imaginary parts of $\tilde{\psi}=A+iB$ are

$$\partial_tA=(s-1)A-2\omega B-(A^2+B^2)A+\nabla^2(A-bB), \quad (4)$$

$$\partial_tB=-(s+1)B-(A^2+B^2)B+\nabla^2(B+bA), \quad (5)$$

where $s^2=\gamma^2-\omega^2$.

II. STABILITY OF UNIFORM STATES

At $s<1$, Eqs. (4) and (5) have only one trivial uniform state $A=0$, $B=0$. At $s>1$, two new uniform states appear: $A=\pm\sqrt{s-1}, B=0$. The onset of these states corresponds to the period doubling of the layer flights sequence, as observed in experiments [2], and predicted by the simple inelastic ball model [2,19]. Signs $\pm$ reflect two relative phases of layer flights with respect to container vibrations [20].

The trivial flat state $A=B=0$ loses stability if the following condition is fulfilled (compare with Ref. [14]):

$$\gamma^2>\frac{(\omega+b)^2}{1+b^2}. \quad (6)$$

Because of the symmetry of Eq. (3), small perturbations from the trivial state lead to the formation of a periodic sequence of rolls or stripes.

Let us analyze the stability of the nontrivial states $A=\pm\sqrt{s-1}$ and $B=0$ with respect to small perturbations with wave number k:

$$\begin{pmatrix}A\\B\end{pmatrix}=\begin{pmatrix}\pm\sqrt{s-1}\\0\end{pmatrix}+\begin{pmatrix}U_k\\V_k\end{pmatrix}\exp[\lambda(k)t+ikx]. \quad (7)$$

The uniform state loses its stability with respect to periodic modulations with the critical wave number k_c at $s<s_c$ (correspondingly, $\gamma<\gamma_c$), where

$$s_c=\frac{\sqrt{(1+\omega^2)(1+b^2)}-\omega+b}{2b}, \quad (8)$$

$$k_c^2=-\frac{2s-1-\omega b}{1+b^2}. \quad (9)$$

Small perturbations in every direction of the wave vector grow at the same rate. The resultant selected pattern is determined by the nonlinear competition between the modes. In the presence of the reflection symmetry $\psi\to-\psi$, quadratic nonlinearity is absent, and cubic nonlinearity near the trivial state favors stripes corresponding to a single mode. Near the fixed points $A=\pm\sqrt{s-1}, B=0$ the reflection symmetry for perturbations $U\to-U, V\to-V$ is broken, and hexagons emerge at the threshold of the instability. To clarify this point we perform a weakly nonlinear analysis of Eqs. (4) and

(5) for $s=s_c-\epsilon$ and $\epsilon \ll 1$. At $\epsilon \to 0$, the variables U and V are related as in a linear system:

$$\begin{pmatrix} U \\ V \end{pmatrix} = \begin{pmatrix} 1 \\ \eta \end{pmatrix} \Psi, \qquad \Psi = \sum A_j \exp[i\mathbf{k}\cdot\mathbf{r}] + \text{c.c.}, \tag{10}$$

where $|k|=k_c$ and $\eta=[2(s_c-1)+k_c^2]/(bk_c^2-2\omega)$.

The corresponding adjoint eigenvector is

$$\begin{pmatrix} U^+ \\ V^+ \end{pmatrix} = \begin{pmatrix} 1 \\ \eta^+ \end{pmatrix}, \tag{11}$$

where $\eta^+=-[2(s_c-1)+k_c^2]/bk_c^2$. Substituting Eq. (10) into Eqs. (4) and (5) and performing the orthogonalization, we obtain equations for the slowly varying complex amplitudes A_j, $j=1$, 2, and 3 (we assume only three waves with triangular symmetry, favored by quadratic nonlinearity):

$$\partial_t A_j = 2\epsilon A_j + a_2 A_{j+1}^* A_{j-1}^* - a_3[|A_j|^2 + 2(|A_{j-1}|^2 + |A_{j+1}|^2)]A_j, \tag{12}$$

where the coefficients a_2 and a_3 are

$$a_2 = \pm 2\sqrt{s-1}\left(2+\frac{1+\eta^2}{1+\eta\eta^+}\right), \quad a_3 = 3(1+\eta\eta^+). \tag{13}$$

Equations (12) were well studied (see Ref. [21]). There exist three critical values of ϵ: $\epsilon_A=-a_2^2/40a_3$, $\epsilon_R=a_2^2/2a_3$, and $\epsilon_B=2a_2^2/a_3$. Hexagons are stable for $\epsilon_A<\epsilon<\epsilon_B$, and stripes are stable for $\epsilon>\epsilon_R$. Thus, near $s=s_c$ the model exhibits stable hexagons [22]. Since we have two symmetric fixed points, both up and down hexagons coexist. For smaller s stripes are stable, and for larger s flat layers are stable, in agreement with observations [3,16], as well as direct numerical simulations of Eq. (3) [23]. The above analysis requires the values of $\epsilon_{A,B,R}$ to be small. For parameters $\omega, b = O(1)$, this requirement is satisfied for ϵ_A, but not for $\epsilon_{B,R}$. The estimates can be improved by substituting $s=s_c+\epsilon$ instead of $s=s_c$ in Eq. (13). The resulting range of stable hexagons is plotted in the phase diagram (ω,γ) (see Fig. 7 below).

III. INTERFACE SOLUTION

At $s>1$, Eqs. (4) and (5) have an interface solution connecting two uniform states $A=\pm\sqrt{s-1}$, $B=0$. Let x be the coordinate perpendicular to the interface and y the parallel coordinate. The interface is the stationary solutions to Eqs. (4) and (5):

$$\begin{aligned} (s-1)A_0 - 2\omega B_0 - (A_0^2+B_0^2)A_0 + A_{0xx} - bB_{0xx} = 0, \\ -(s+1)B_0 - (A_0^2+B_0^2)B_0 + B_{0xx} + bA_{0xx} = 0. \end{aligned} \tag{14}$$

For $b=0$, Eqs. (14) have a solution of the form $A_0=\pm\sqrt{s-1}\tanh(\sqrt{s-1}x/2), B_0=0$. For $b\neq 0$ the solution is available only numerically. We used the shooting matching technique to find this solution in the range of parameters ω, b, and γ. A typical solution is shown in Fig. 1. As one sees from the figure, for $b\neq 0$ the asymptotic behavior of the interface exhibits decaying oscillations.

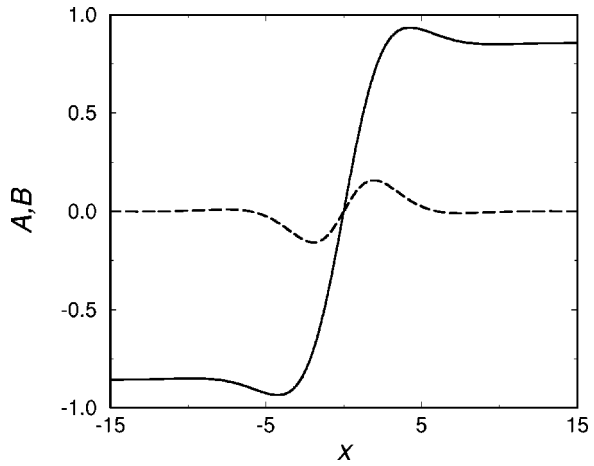

FIG. 1. Interface solution to Eqs. (14) obtained numerically for $\omega=1$, $b=4$, and $\gamma=2$. The solid line corresponds to A and the dashed line to B, respectively.

Let us now consider the perturbed solution

$$\begin{pmatrix} A \\ B \end{pmatrix} = \begin{pmatrix} A_0 \\ B_0 \end{pmatrix} + \begin{pmatrix} \tilde{A}(x) \\ \tilde{B}(x) \end{pmatrix} \exp[\lambda(k)t + iky], \tag{15}$$

where k is the transverse modulation wave number and $\lambda(k)$ is the corresponding growth rate. For $\tilde{A}$ and $\tilde{B}$ we obtain the linear equation

$$\hat{L}\begin{pmatrix} \tilde{A} \\ \tilde{B} \end{pmatrix} = [\lambda(k)+k^2]\begin{pmatrix} \tilde{A} \\ \tilde{B} \end{pmatrix} + bk^2\begin{pmatrix} \tilde{B} \\ -\tilde{A} \end{pmatrix}, \tag{16}$$

where the matrix $\hat{L}$ is of the form

$$\hat{L} = \begin{pmatrix} s-1-3A_0^2-B_0^2+\partial_x^2 & -2\omega-2A_0B_0-b\partial_x^2 \\ -2A_0B_0+b\partial_x^2 & -s-1-A_0^2-3B_0^2+\partial_x^2 \end{pmatrix}. \tag{17}$$

In order to determine the spectrum of eigenvalues $\lambda(k)$ we have solved Eq. (16) along with stationary equations (14) numerically using numerical matching-shooting technique. We have found that for small ω the interface is stable with respect to transverse undulations, i.e., $\lambda(k)\leqslant 0$. However, for the values of ω above certain critical value $\omega_c(\gamma,b)$ the interface exhibits transverse instability: $\lambda(k)>0$ in the band of wave numbers $|k|<k_c$; see Fig. 2.

This instability is confirmed by direct numerical simulations of Eq. (3). An example of the evolution of slightly perturbed interface is shown in Fig. 4. Small perturbations grow to form a ''decorated'' interface. With time these decorations evolve slowly, and eventually form a labyrinthine pattern.

The neutral curve for this instability can be determined as follows. Numerical analysis shows that at the threshold the most unstable wave number is $k=0$, and we can expect that, for $k\to 0$, $\lambda\sim k^2$; see Fig. 2. Expanding Eq. (16) in a power series of k^2,

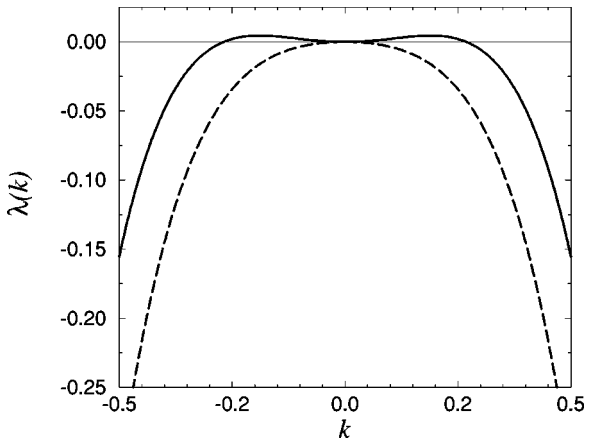

FIG. 2. Spectrum of eigenvalues $\lambda(k)$ for $\omega=1.3$, $b=4$, and $\gamma=2$ (solid line) and $\omega=1$, $b=4$, and $\gamma=2$ (dashed line) obtained from numerical solution of Eq. (16).

$$\begin{pmatrix}\tilde{A}\\ \tilde{B}\end{pmatrix}=\begin{pmatrix}A^{(0)}\\ B^{(0)}\end{pmatrix}+k^2\begin{pmatrix}A^{(1)}\\ B^{(1)}\end{pmatrix}+\cdots, \tag{18}$$

in the zeroth order in k we obtain $\hat{L}(A^{(0)},B^{(0)})=0$. The corresponding solution is the translation mode $A^{(0)}=\partial_x A_0(x), B^{(0)}=\partial_x B_0(x)$. In the first order in k^2 we arrive at the linear inhomogeneous problem

$$\hat{L}\begin{pmatrix}A^{(1)}\\ B^{(1)}\end{pmatrix}=[\lambda(k)+k^2]\begin{pmatrix}A^{(0)}\\ B^{(0)}\end{pmatrix}+bk^2\begin{pmatrix}B^{(0)}\\ -A^{(0)}\end{pmatrix}. \tag{19}$$

A bounded solution to Eq. (19) exists if the right-hand side is orthogonal to the localized mode of the adjoint operator $A^{\dagger},B^{\dagger}$. The adjoint operator $\hat{L}^{\dagger}$ is of the form

$$\hat{L}^{\dagger}=\begin{pmatrix}s-1-3A_0^2-B_0^2+\partial_x^2 & -2A_0B_0+b\partial_x^2\\ -2\omega-2A_0B_0-b\partial_x^2 & -s-1-A_0^2-3B_0^2+\partial_x^2\end{pmatrix}. \tag{20}$$

Since the operator $\hat{L}^{\dagger}$ is not self-adjoint, the adjoint mode does not coincide with the translation mode, and, therefore, must be obtained numerically.

The orthogonality condition fixes the relation between λ and k:

$$\lambda=-\sigma k^2, \quad \sigma=1+b\frac{\int_{-\infty}^{\infty}[A^{(0)}B^{\dagger}-B^{(0)}A^{\dagger}]dx}{\int_{-\infty}^{\infty}[A^{(0)}A^{\dagger}+B^{(0)}B^{\dagger}]dx}, \tag{21}$$

where σ is ''surface tension'' of the interface. The instability, corresponding to the negative surface tension of the interface, onsets at $\sigma=0$. Although the interface solution $A(x)$ is not localized (see Fig. 1), the integrals in Eq. (21) converge because the adjoint functions $A^{\dagger}$ and $B^{\dagger}$ are localized. The numerically obtained adjoint eigenmode is shown in Fig. 3. The neutral curve is shown in Fig. 7. Direct numerical simulations of Eq. (3) show that this instability leads to so called ''decorated'' interfaces [see Fig. 4(a)]; however, at later stages the undulations grow and finally form labyrinthine patterns (Figs. 4(b)–4(d)].

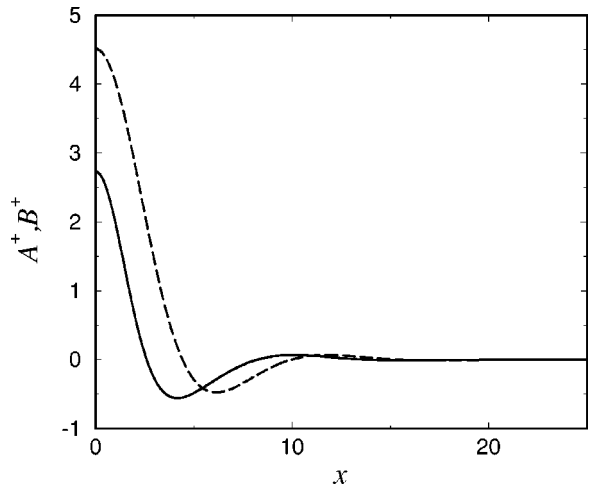

FIG. 3. Adjoint eigenfunction obtained numerically for $\omega=1.3$, $b=4$, and $\gamma=2$. The solid line corresponds to $A^{\dagger}$ and the dashed line to $B^{\dagger}$, respectively.

The emergence of the labyrinthine patterns as a result of interface instability contradicts experiments [4,5,16] where stable decorated interfaces are typically observed. Thus the model [Eq. (3)] does not capture saturation of the interface instability and requires modification. We also checked that the coupling to the density field introduced in Ref. [14] does not provide desired saturation.

Let us now discuss possible mechanisms of saturation of the transverse instability of the interface, which is not captured by Eq. (3). The reason for the proliferation of the labyrinths is that local stabilization mechanisms cannot saturate the ''negative surface tension instability'' of the interface. Indeed, the behavior of the small perturbation ζ of an almost flat interface is described by the linear equation $\zeta_t=-\sigma\Delta\zeta$, where σ is the surface tension. The linear growth must be counterbalanced by nonlinear terms. Due to translation invariance the local nonlinearity can be a function of gradients of ζ only. In the lowest order the first term is $|\nabla\zeta|^3$, since the quadratic term does not saturate the monotonic instability.

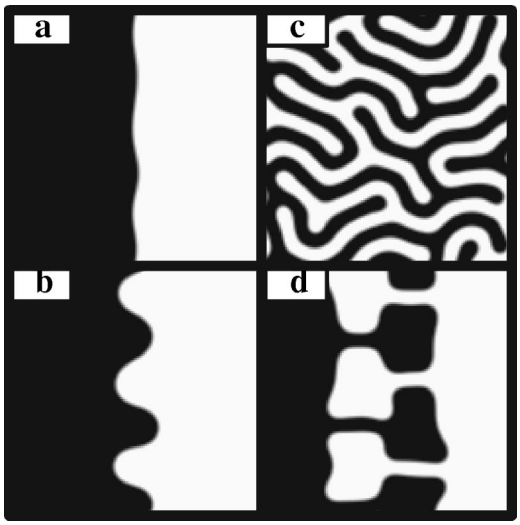

FIG. 4. (a)–(d) Interface instability and labyrinth formation [Eq. (3)]. $\omega=2$, $b=4$, and $\gamma=2.9$, the domain size is 100×100 units, and snapshots are taken at times $t=1000$, 1600, 2300, and 4640.

Since for the modulation wave number $k \to 0$ one has $|\nabla \zeta|^3 \sim k^2 |\zeta|^3$ and $\Delta \zeta \sim k^2 \zeta$, the linear instability always overcomes the local nonlinearity at small wave numbers. As a result, small perturbations grow and saturation occurs due to nonlocal interactions as in a labyrinthine pattern which is stabilized by nonlocal repulsion of the fronts (see Ref. [24]).

As we see in our model, the interface instability does not result in stable decorated interfaces. One possibility for the saturation of this instability could be local convection induced by the interface. Indeed, due to the shear motion of grains at the interface (the flat regions move in antiphase) local convective flow can be created. The scale of this flow can be larger than the interface thickness. One of the possible manifestations of the convection beside grain transport is a reduction of the effective ''viscosity'' of the flat layer, or an increase in the sensitivity to external vibrations [25]. As we can see from Fig. 7, an increase in vibration magnitude γ suppresses the interface instability. As the instability develops, the length of the interface grows, which increases the convection and finally suppresses the instability. This feedback mechanism results in a saturation of the interface instability, and creates stable decorations.

Although the details of this coupling are not yet known, it can be implemented within the order-parameter approach in a phenomenological way. In Eq. (3) the forcing $\gamma\psi^*$ must be replaced by $(\gamma_0 + w)\psi^*$, where w includes the effect of local convective flow and $\gamma_0 = \text{const}$. We take the simplest possible form of the coupling to the convective flow,

$$w = \frac{\epsilon}{S} \int dr' \exp\left(-\frac{|r - r'|^2}{r_0^2} \right) |\nabla \psi(r')|^2, \qquad (22)$$

where r_0 characterizes the typical scale of the convective flow, ϵ is the amplitude of the coupling, and S is the area of integration domain. Since $|\nabla \psi(r')|$ is nonzero only at the interface, this integral is proportional to the total length of the interface. With the growth of the interface length the value of the ''effective forcing'' $\gamma = \gamma_0 + w$ grows as well, and eventually leaves the instability domain.

We performed numerical simulations with Eq. (3) modified in the following way. The convolution integral (22) was calculated using the fast Fourier transform. The results are presented in Fig. 5. Remarkably, for a certain range of parameters the instability indeed saturates due to the nonlocal term [Eq. (22)], and we find interfaces with stable decorations; see Fig. 5(a).

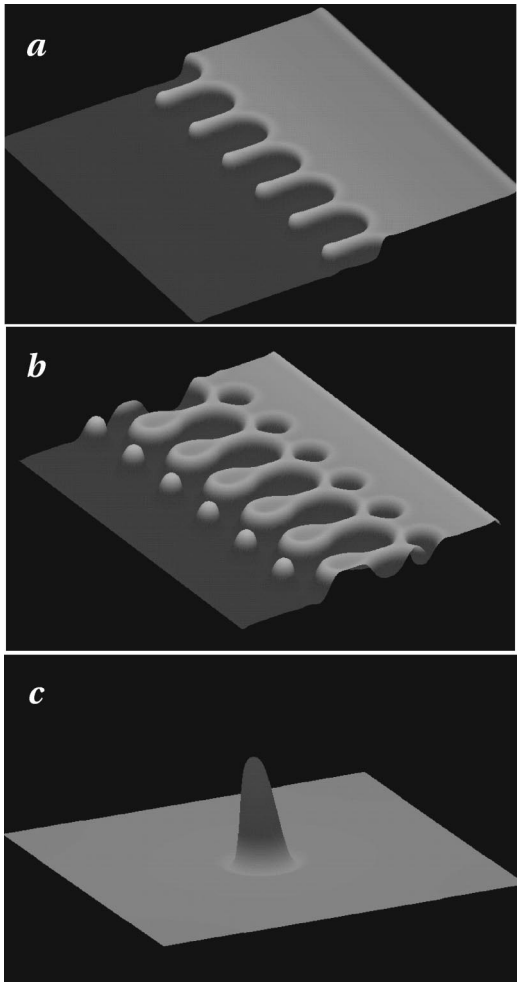

FIG. 5. Computer simulations of modified Eq. (3). Surface plots show $\mathrm{Re}\,\Psi$ for different stationary solutions: (a) A saturated interface; $\omega = 1.2$, $\gamma = 1.85$, $b = 4$, $\epsilon = 0.002$, $r_0 = 40$, and $L = 160$. (b) A saturated interface with bound *superoscillons*; $\omega = 1.2$, $\gamma = 1.75$, $b = 4$, $\epsilon = 0.002$, $r_0 = 40$, and $L = 160$. (c) A single *superoscillon* at $\omega = 1.2, \gamma = 2.2, b = 4$, $\epsilon = 0.002$, $r_0 = 40$, and $L = 100$.

IV. LOCALIZED SOLUTIONS

In addition to the interface solution which exists for $s > 1$, for even higher values of s Eq. (3) possesses a variety of other nontrivial two dimensional solutions including localized superoscillons. A typical solution and its corresponding localized linear mode are shown in Fig. 6.

Although super-oscillons appears to be similar to the ''conventional oscillon'' discovered in Ref. [4], there is a significant difference. The asymptotic behavior of the superoscillon is $\Psi \to A_0 \neq 0$ for $r \to \infty$, whereas the regular oscillon has $\Psi \to 0$. This implies that the phase of the superoscillon is always locked into the phase of the flat layerexhibiting *period-doubled behavior*, whereas ''conventional oscillons'' of either phase coexist on the *harmonic* background (the amplitude of period 2 oscillations is zero). As a result oppositely phased superoscillons must be separated by an interface connecting two opposite phases of the period-doubled flat layer, whereas oppositely phased oscillons can easily form stable bound states (dipoles [4]).

Superoscillons, in the presence of additional subharmonic driving, are somewhat similar to normal oscillons of like polarity (see Ref. [4]). In this case the external driving creates a period-doubled background of the flat layer, and locks the phase of the superoscillons. However, superoscillons exist for parameter values where the oscillons of Ref. [4] are impossible even with additional subharmonic driving.

Superoscillons exist in a relatively narrow domain of parameters of Eq. (3). A decrease of γ leads to a destabilization of the localized eigenmode leading to a subsequent nucleation of new ''superoscillons'' on the periphery of the unstable superoscillon; with an increase of γ superoscillons disappear in a saddle-node bifurcation.

For certain values of γ_0 we also find an interesting structure consisting of a decorated interface and a chain of superoscillons bound to the decorations; see Fig. 5(b). These

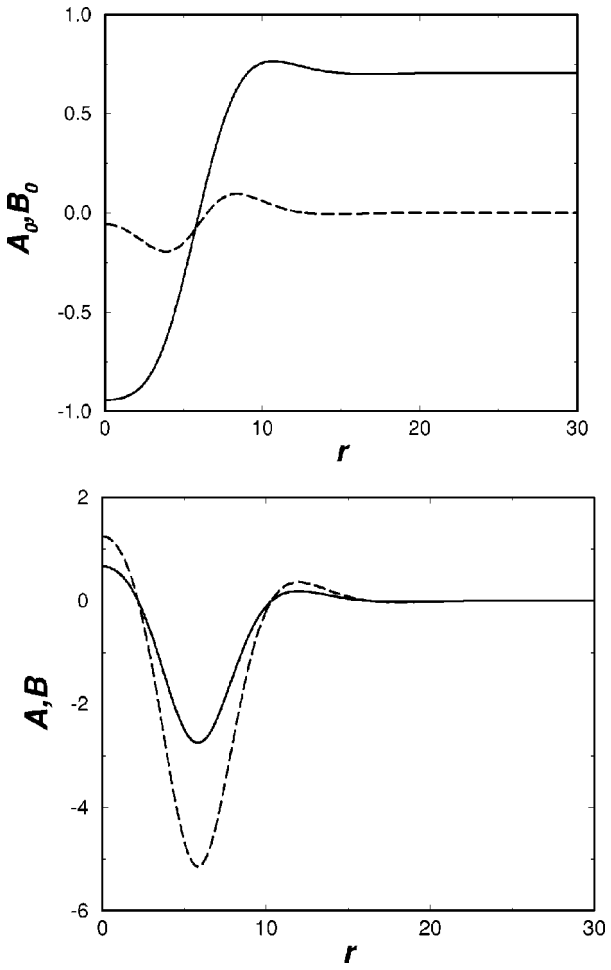

FIG. 6. (a) Axisymmetric localized solution (superoscillon) obtained for $b=4$, $\omega=1$, and $\gamma=1.8$ for Eq. (3) at $b=4$. *A*, solid line; *B*, dashed line. (b) Localized eigenfunction corresponding to the maximum eigenvalue $\lambda=-0.0009$.

objects can exist completely independently of the interface [Fig. 5(c)], as one may expect for Eq. (3). Thus we conclude that the extended equation (3) qualitatively describes the observed phenomenology.

V. PHASE DIAGRAM

The results of a linear stability analysis can be summarized in the phase diagram shown in Fig. 7. Remarkably, the structure of the phase diagram of Fig. 7 is qualitatively similar to that of experiments for high frequencies of vibration; see Fig. 10 and Refs. [2–5,10,16]. Increasing the vibration amplitude γ leads to a transition from a trivial state to stripes, hexagons, decorated interfaces, and, finally, to stable interfaces. A transition from unstable to stable interfaces also occurs with decreasing ω (increasing vibration frequency f), in agreement with Refs. [16,26]. In experiments at still higher Γ's, quarter-harmonic patterns appear; however, these patterns are not described by our model. Our analysis also predicts the coexistence of stripes and hexagons in a very narrow parameter range (see Sec. II). Superoscillons were found in a narrow domain close to line 7 of Fig. 7.

Note that square patterns, which emerge at lower frequencies, are not included in the phase diagram. They are obtained within the full model of Eqs. (1) and (2), with an additional density field ρ; see Ref. [14].

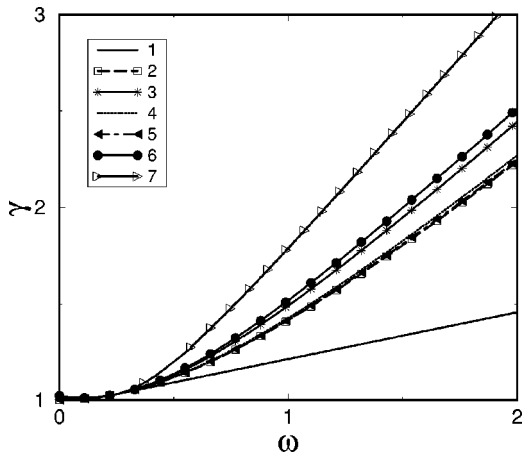

FIG. 7. Phase diagram for Eq. (3) at $b=4$. Line 1, $\gamma^2=(\omega+b)^2/(1+b^2)$; line 2, $s^2\equiv\gamma^2-\omega^2=1$; line 3, $s=s_c$; line 4, $s=s_c-\epsilon_R$; line 5, $s=s_c-\epsilon_B$; line 6, $s=s_c-\epsilon_A$; line 7, surface tension $\sigma=0$. Below line 1 there are no patterns. Between lines 1 and 4, stripes are stable. Between lines 5 and 6, hexagons are stable. Above line 2, nontrivial flat states exist. Above line 3 these states are stable. Interfaces are unstable below line 7. Hexagons and stripes coexist between lines 4 and 5.

VI. SWIFT-HOHENBERG EQUATION

Near the line $s=1$ (see Fig. 7) Eq. (3) can be simplified. In the vicinity of this line $A\sim(s-1)^{1/2}$ and $B\sim(s-1)^{3/2}\ll A$. In leading order we can obtain $B=b\nabla^2 A/2$ from Eq. (5), and Eq. (4) yields [27]

$$\partial_t A=(s-1)A-A^3+(1-\omega b)\nabla^2 A-\frac{b^2}{2}\nabla^4 A. \quad (23)$$

Rescaling the variables $t\to(s-1)t$, $A\to(s-1)^{-1/2}A$, $x\to[2(s-1)/b^2]^{1/4}$, we arrive at the Swift-Hohenberg equation (SHE)

$$\partial_t A=A-A^3-\delta\nabla^2 A-\nabla^4 A, \quad (24)$$

where

$$\delta=\frac{\omega b-1}{b}\sqrt{\frac{2}{s-1}}. \quad (25)$$

The description by the SHE is valid if $\delta\sim O(1)$, which implies an additional condition for the validity of this approach $\omega b-1\ll 1$ at $s\to 1$.

Although this equation is simpler than Eq. (3), it captures many essential features of the original system dynamics, including the existence and stability of stripes and hexagons in different parameter regions (see Refs. [28,29]); the existence of the interface solutions, interface instability, and superoscillons; and the emergence of labyrinthine patterns [30]. Indeed, a simple analysis shows that the growth rate of the instability of the uniform state $A=1$ as a function of the perturbation wave number is determined by the formula $\lambda(k)=-2+\delta k^2-k^4$; it becomes unstable at $\delta>\delta_c=2\sqrt{2}$ at a critical wave number $k_c=\sqrt{2}$. As in the original model,

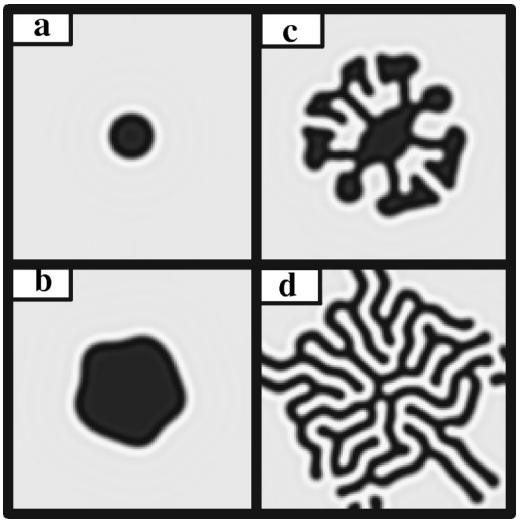

FIG. 8. (a)–(d) Labyrinth formation from a circular spot (SHE); $\delta=1.4$, the domain size is 100×100 units, and $t=200$, 1300, 1700, and 1900.

near the threshold of this instability, subcritical hexagonal patterns are preferred. The interface stability can also be analyzed more simply, as the linearized operator corresponding to model (24) is self-adjoint. The threshold value of δ is obtained from the solvability condition

$$\int_{-\infty}^{\infty}(\delta_{\rm th}A_{0x}^2-2A_{0xx}^2)dx=0, \tag{26}$$

which yields $\delta_{\rm th}=1.011$. This yields an equation for the neutral curve of the interface instability in the Swift-Hohenberg limit in the form

$$s=1+\frac{2(\omega b-1)^2}{\delta_{\rm th}^2 b^2}. \tag{27}$$

Figures 8(a)–8(d) show the development of the interface instability within the SHE with a subsequent transition to labyrinthine patterns, similar to the dynamics of the full parametric equation (3). Again, to saturate the instability, an additional nonlocal mechanism is required.

As was shown recently, the Swift-Hohenberg equation also possesses localized solutions (see Refs. [30,31]). These localized states are analogous to the superoscillons of Eq. (3).

VII. SUBHARMONIC FORCING AND INTERFACE MOTION

Now we will focus on the effect of additional subharmonic driving on the motion of the interface. In the original model [Eq. (3)], the interface does not move due to symmetry between the left and right halves of the interface. However, if the plate oscillates with two frequencies f and $f/2$, the symmetry between these two states, connected by the interface, is broken, and the interface moves. The velocity of the interface motion depends on the relative phase of the subharmonic forcing with respect to the forcing at f. The effect of a small external subharmonic driving applied in the background of the primary harmonic driving with the frequency f can be described by the equation [cf. Eq. (3)]

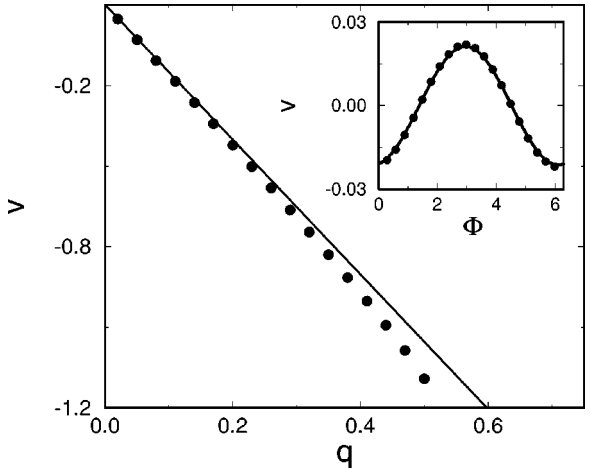

FIG. 9. Interface velocity v for $\omega=1$, $b=4$, and $\gamma=2.5$ vs q at $\Phi=0$. Inset: v vs Φ at $q=0.01$. (●), numerical results; (—), analytical expression (30).

$$\partial_t\psi=\gamma\psi^*-(1-i\omega)\psi+(1+ib)\nabla^2\psi-|\psi|^2\psi+qe^{i\Phi}, \tag{28}$$

where q characterizes the amplitude of the subharmonic pumping, and Φ determines its relative phase.

For small q, we look for a moving interface solution in the forms $\psi=\psi_0(x-vt)+q\psi_1(x-vt)+\cdots$ and $v=O(q)$, or, alternatively,

$$\begin{pmatrix}A\\B\end{pmatrix}=\begin{pmatrix}A_0(x-vt)\\B_0(x-vt)\end{pmatrix}+q\begin{pmatrix}a(x-vt)\\b(x-vt)\end{pmatrix}+O(q^2). \tag{29}$$

The solvability condition [compare with Eq. (21)] fixes the interface velocity as a function of the amplitude and phase of the external subharmonic driving,

$$v=-q\frac{\cos\Phi\int A^\dagger dx+\sin\Phi\int B^\dagger dx}{\int(A^\dagger\partial_x A_0+B^\dagger\partial_x B_0)dx}=q\alpha\sin(\Phi-\Phi_0), \tag{30}$$

where $\alpha=$const is the susceptibility of the interface for external forcing, and $\Phi_0=$const is some phase shift. An explicit answer is obtained for $b=0$ when $A^\dagger=\partial_x A_0$ and $\Phi=0,\pi$, which yields the interface velocity $v=\mp\frac{3}{2}qA_0^{-2}=\mp\frac{3}{2}q(s-1)^{-1}$. In general, A, B, $A^\dagger$, and $B^\dagger$, and hence v, can be found numerically. The interface velocity as function of q,Φ is shown in Fig. 9.

Thus from this analysis we conclude that additional subharmonic driving results in a controlled motion of the interface. The velocity of the interface depends on the amplitude of the driving, and the direction is determined by the relative phase Φ.

VIII. EXPERIMENTAL RESULTS

We performed experiments with a thin layer of granular material subjected to periodic driving. Our experimental

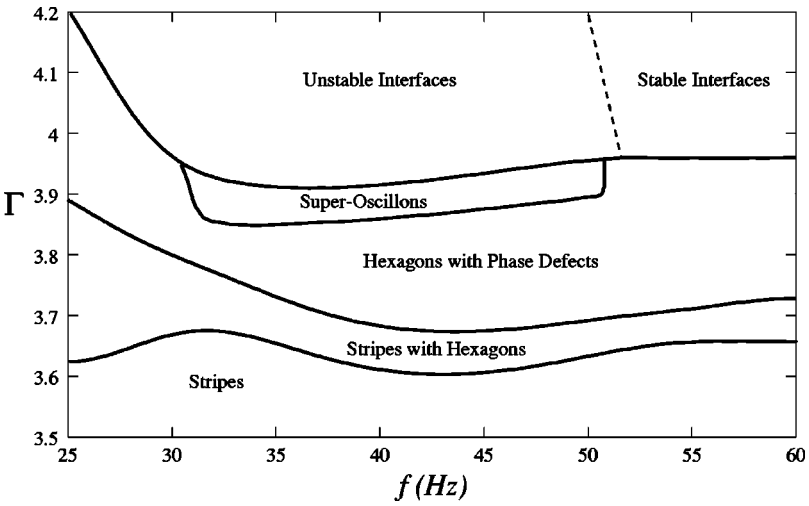

FIG. 10. Phase diagram. The material is 150-μm copper balls, and the layer thickness is ten particle diameters.

setup is similar to that of Ref. [5]. We used 0.15-mm-diameter bronze or copper balls, and the layer thickness in our experiments was ten particles. We performed experiments in a rectangular cell of 4×12 cm^2. We were able to vary the acceleration Γ and frequency f of the primary driving signal as well as the acceleration γ, frequency f_1 and phase Φ of the secondary (additional) driving signal. The interface position and vertical accelerations were acquired using high-speed video and accelerometers, and further analyzed on a Pentium computer. To maintain and measure the proper acceleration at f and $f/2$ we employed the lock-in technique with our signal originating from an accelerometer attached to the bottom of the cell. This allowed for simultaneous *real-time* feedback and control of the device. To reduce the interstitial gas effects [32] we reduced the pressure to 2 mTorr. Our visual data were acquired using a high-speed digital camera (Kodak SR-1000c), in addition to high-speed recording this also allowed for a synchronization between the patterns and the image acquisition.

A. Phase diagram

The experimental phase diagram is shown in Fig. 10. It is similar to that of Refs. [3,4,16]; however, the transition from hexagons to interfaces is elaborated in more detail. There is a small hysteresis at the transition line from stripes to hexagons (not shown in the phase diagram). The dashed line indicates the stability line for interfaces with respect to periodic undulations, determined as the average half-width of the pattern. To determine this stability limit, we kept the value of acceleration Γ fixed and increased the driving frequency f. For each value of the frequency we extracted the interface width by averaging up to ten images of the interface. In order to find that amplitude of the periodic undulations l we subtracted the thickness of the flat interface l_0 from the obtained value. The resultant amplitude or undulations l as functions of driving frequency f are shown in Fig. 11. As one sees from the figure, the amplitude of undulations l decreases gradually, approaching the critical value of the frequency. However, a small hysteresis at the transition point cannot be excluded because of large error bars.

As follows from the phase diagram, for a small amplitude of the vertical acceleration $\Gamma<3.6$ stripes are the only stable pattern (note that we focus on high-frequency patterns when squares do not exist; compare Ref. [3]). At slightly higher values ($\Gamma=3.6$–3.7) stripes and hexagons coexist. For higher values ($\Gamma=3.7$–4.0) the hexagons become stable. Due to the subharmonic character of motion both up and down hexagons may coexist, separated by a line phase defect [Fig. 12(a)]. There exists a narrow band, from $\Gamma=3.85$ to 4.0, where localized states, or *superoscillons*, appear both within the bulk of the material and also pinned to the front between the interface and the bulk [Fig. 12(b)]. For even higher values of the acceleration $\Gamma>4.0$ the superoscillons disappear [Fig. 12(c)], leading to isolated interfaces with periodic decorations.

B. Controlled motion of interface

In the absence of additional driving the interface drifts toward the middle of the cell (see Fig. 12). We attribute this effect to the feedback between the oscillating granular layer and the plate vibrations, due to the finite ratio of the mass of the granular material to the mass of the vibrating plate. Even in the absence of subharmonic drive, the vibrating cell can acquire subharmonic motion from the periodic impacts of the granular layer on the bottom plate at half the driving frequency. If the interface is located in the middle of the cell, the masses of material on both sides of the interface are equal, and, due to the antiphase character of the layer motion

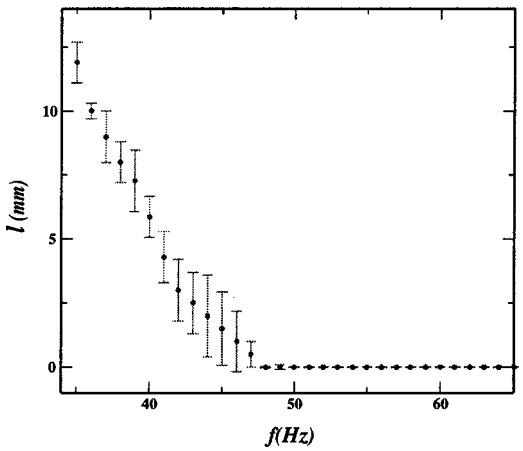

FIG. 11. The amplitude of periodic undulations l as a function of driving frequency f. The acceleration amplitude is $\Gamma=4.1$.

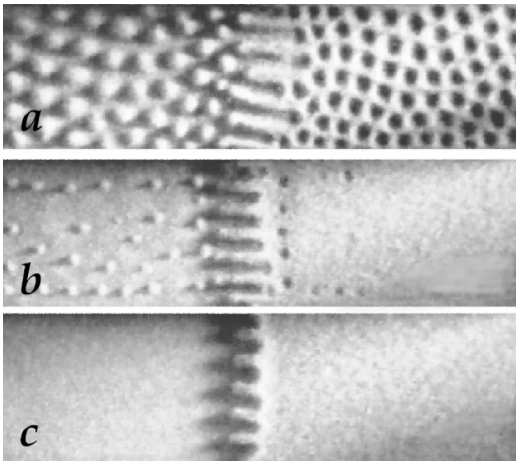

FIG. 12. Representative high-acceleration patterns in the rectangular 4×12-cm cell, driving frequency $f=40$ Hz: (a) $\Gamma=3.75$ shows the onset of the *interface* with up and down hexagons. (b) $\Gamma=3.94$ *superoscillons* are present in the flat layer and are pinned to the front near the interface. (c) $\Gamma=4$, isolated decorated interface.

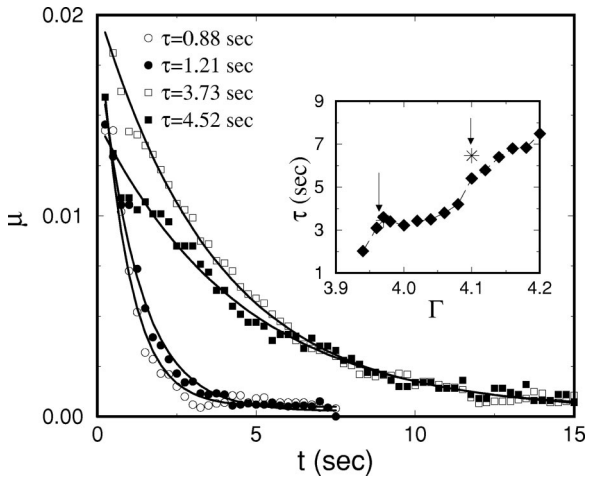

FIG. 13. Amplitude of the subharmonic acceleration μ of the cell averaged over four measurements vs time for the interface propagating to the center of the cell for $\Gamma=3.97$ and $f=40$ Hz. Circles and squares correspond to circular and rectangular cells, and open and closed symbols correspond to light and heavy cells, respectively. Heavy cells differ from light ones by an additional weight of 250 g attached to the moving shaft. Solid lines show an exponential fit $\mu\sim\exp(t/\tau)+$const. Inset: τ vs Γ for light rectangular cell.

on both sides, an additional subharmonic driving is not produced. The displacement of the interface X from the center of the cell leads to a mass difference Δm on opposite sides of the interface, which in turn causes an additional subharmonic driving proportional to Δm. In a rectangular cell, $\Delta m\propto X$. Our experiments show that the interface moves in such a way to decrease the subharmonic response, and the feedback provides an additional term $-X/\tau$ on the right-hand side of Eq. (30), yielding

$$\frac{dX}{dt}=-X/\tau+q\alpha\sin(\Phi-\Phi_0). \tag{31}$$

The relaxation time constant τ depends on the mass ratio (this also holds for the circular cell if X is small compared to the cell radius). Thus, in the absence of an additional subharmonic drive ($q=0$), the interface will eventually divide the cell into two regions of equal area (see Fig. 12).

In order to verify the prediction of Eq. (31) we performed the following experiment. We positioned the interface off center by applying an additional subharmonic drive. Then we turned off the subharmonic drive and immediately measured the amplitude μ of the plate acceleration at the subharmonic frequency [33]. The results are presented in Fig. 13. The subharmonic acceleration of the cell decreases exponentially as the interface propagates to the center of the cell. The measured relaxation time τ of the subharmonic acceleration increases with the mass ratio of the granular layer and of the cell with all other parameters fixed. The mass of the granular layer was varied by using two different cell sizes—circular, diameter 15.3 cm, and rectangular, 4×12 cm—while keeping the thickness of the layer unchanged. For these cells we found that the relaxation time τ in the rectangular cell is about four times greater than for the circular cell (see Fig. 13). This is consistent with the ratio of the total masses of granular material (52 grams in rectangular cell and 198 grams in the circular cell). In a separate experiment the mass of the cell was changed by attaching an additional weight of 250 grams to the moving shaft, which weighs 2300 grams. This led to an increase of the corresponding relaxation times of 15–25 %. The relaxation time τ increases rapidly with Γ (see the inset of Fig. 13).

When an additional subharmonic driving is applied, the interface is displaced from the middle of the cell. For small amplitude of the subharmonic driving γ, the stationary interface position is $X=q\alpha\tau\sin(\Phi-\Phi_0)$, since the restoring force balances the external driving force. The equilibrium position X as function of Φ is shown in Fig. 14(a). The solid line depicts the sinusoidal fit predicted by the theory. Because of the finite mass ratio effect, the amplitude of the measured plate acceleration μ at frequency f_1 also shows periodic behavior with Φ [see Fig. 14(b)], enabling us to infer the interface displacement from the acceleration measurements.

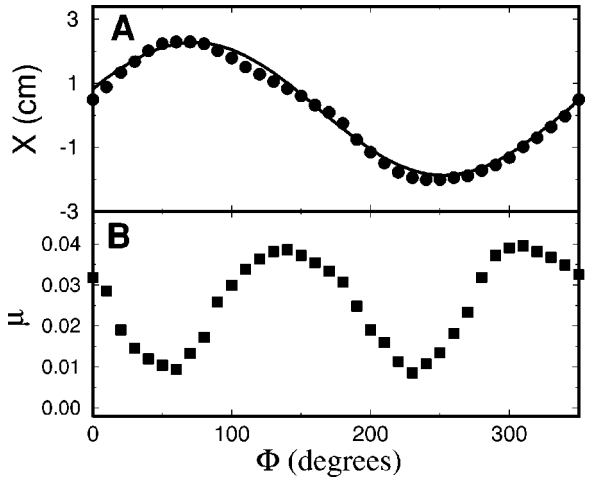

FIG. 14. (a) Equilibrium position X and (b) amplitude of measured subharmonic acceleration μ as functions of phase Φ. Circular cell: $\Gamma=4.1$, $f=40$ Hz, and $q=1.25\%$ of Γ.

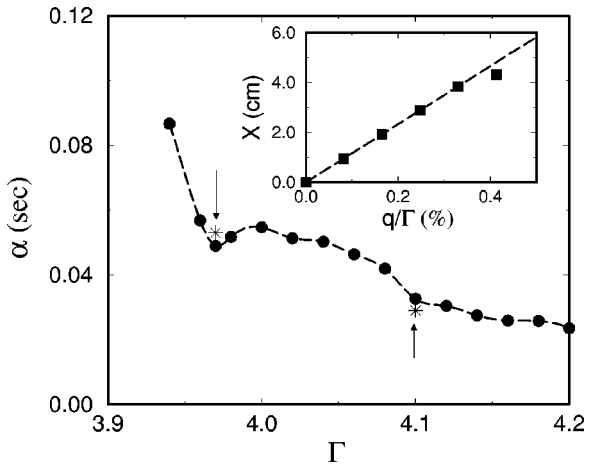

FIG. 15. Susceptibility α vs Γ at $f=40$ Hz, rectangular cell. Inset: displacement X as a function of q at $\Phi=260^0$.

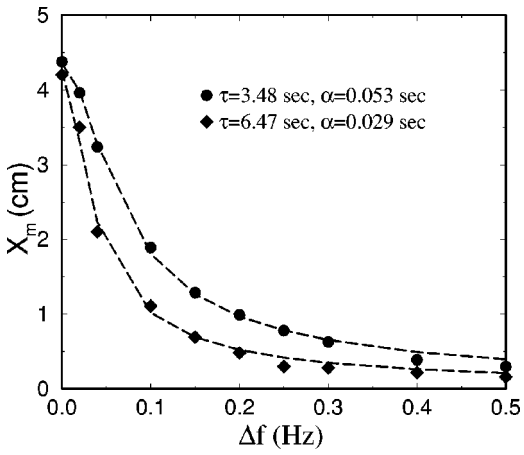

FIG. 16. Maximum displacement X_m from the center of the rectangular cell as a function of frequency difference $\Delta f=f_1-f/2$ for $f=40$ Hz, and for $\Gamma=3.97$ (circles) and $\Gamma=4.1$ (diamonds). Dashed lines are fit to $X_m=V_0/\sqrt{\tau^{-2}+(2\pi\Delta f)^2}$. The values of α and τ obtained from the fit are also indicated in Figs. 13 and 15 by arrows with stars.

For an even larger amplitude of subharmonic driving (more than 4–5 % of the primary driving) extended patterns (hexagons) re-emerge throughout the cell.

The velocity $V_0=q\alpha$, which the interface would have in an infinite system, can be found from measurements of the relaxation time τ and maximum displacement X_m at a given amplitude of subharmonic acceleration γ, $V_0=X_m/\tau$; see Eq. (31). We verified that in the rectangular cell the displacement X depends linearly on γ almost up to values at which the interface disappears at the short side wall of the cell (see the inset of Fig. 15). Figure 15 shows the susceptibility α as a function of the amplitude of the primary acceleration Γ. The susceptibility decreases with Γ. The cusplike features in the Γ dependence of α (and τ; see the inset to Fig. 13) are presumably related to the commensurability between the lateral size of the cell and the wavelength of the interface decorations.

We developed an alternative experimental technique which allowed us to measure simultaneously the relaxation time τ and the ''asymptotic'' velocity V_0. This was achieved by a small detuning Δf of the additional frequency f_1 from the exact subharmonic frequency $f/2$, i.e., $\Delta f=f_1-f/2\ll f$. This is equivalent to the linear increase of the phase shift Φ with the rate $2\pi\Delta f$. This linear growth of the phase results in a periodic motion of the interface with frequency Δf and amplitude $X_m=V_0/\sqrt{\tau^{-2}+(2\pi\Delta f)^2}$ [see Eq (31)]. The measurements of the ''response functions'' $X_m(\Delta f)$ are presented in Fig. 16. From the dependence of X_m on Δf we can extract parameters V_0, α, and τ by a fit to the theoretical function. The measurements are in a very good agreement with previous independent measurements of the relaxation time τ and susceptibility α. For a comparison with the previous results, we indicate the values for τ and α, obtained from the response function measurements of Figs. 13 and 15 (stars). The measurements agree within 5%.

CONCLUSIONS

In this paper we studied the dynamics of thin vibrated granular layers in the framework of a phenomenological model based on the Ginzburg-Landau-type equation for an order parameter characterizing the amplitude of subharmonic sand vibrations. Although a rigorous derivation of this model is not possible to date, our approach gives a significant insight into the problem at hand, and results in testable predictions. Our model is complementary to more elaborate fluid-dynamic-like continuum descriptions or direct molecular dynamics simulations, and allows us to carry out analytical calculations of various regimes and predict their stability. A challenging problem is to establish a quantitative relation between our order-parameter model and other models as well as experiments.

We have shown in this paper that the generic parametric Ginzburg-Landau model of Eq. (3) captures not only patterns of vibrated sand near the primary bifurcation, but also large acceleration patterns such as hexagons, interfaces, and superoscillons. The structure of the phase diagram of Fig. 7 for high frequencies and amplitudes of vibrations is qualitatively similar to that of previous experiments (Refs. [2,3,5,16]), as well as the experiments reported here. Increasing the vibration amplitude leads to a transition from a trivial state to stripes, hexagons, decorated interfaces, and finally, to stable interfaces. Interface decorations were found to be a result of the transversal instability of a flat interface, which is analogous to the negative surface tension. We found that Eq. (3) is not sufficient to describe the saturation of the interface instability. We propose a possible nonlocal mechanism of saturation of this instability which takes into account the dependence of the overall length of the interface and the magnitude of parametric forcing, which may occur due to a large scale convective flow induced by the sand motion near the interface. We described analytically the motion of the interface under the symmetry-breaking influence of the small subharmonic driving.

In our experimental study we found that on a qualitative level the theoretical phase diagram is similar to the experimental one. The experiments also confirmed the existence of superoscillons and their bound states with the interface, as predicted by the theory. Further experimental study is necessary to elucidate the specific mechanism for saturation of the interface instability.

Stimulated by the theoretical prediction, we also performed experimental studies of interface motion under additional subharmonic driving. The experiment confirmed that the direction and magnitude of the interface displacement depend sensitively on the amplitude and relative phase of the subharmonic driving. Moreover, we found that the period-doubling motion of the flat layers produces subharmonic driving because of the finite ratio of the mass of the granular layer and the cell. This in turn leads to the restoring force driving the interface toward the middle of the cell.

ACKNOWLEDGMENTS

We thank L. Kadanoff, R. Behringer, H. Jaeger, H. Swinney, and P. Umbanhowar for useful discussions. This research was supported by the U.S. Department of Energy, Grant No. W-31-109-ENG-38, and by NSF, STCS No. DMR91-20000. C.J. acknowledges support from a joint ANL-UofC collaborative grant. L.T. thanks the Engineering Research Program of the Office of Basic Energy Sciences at the U.S. Department of Energy for support under Grant Nos. DE-FG03-96ER14592 and DE-FG03-95ER14516.

[1] H.M. Jaeger, S.R. Nagel, and R.P. Behringer, Phys. Today **49** (4), 32 (1996); Rev. Mod. Phys. **68**, 1259 (1996).
[2] F. Melo, P.B. Umbanhowar, and H.L. Swinney, Phys. Rev. Lett. **72**, 172 (1994).
[3] F. Melo, P.B. Umbanhowar, and H.L. Swinney, Phys. Rev. Lett. **75**, 3838 (1995).
[4] P.B. Umbanhowar, F. Melo, and H.L. Swinney, Nature (London) **382**, 793 (1996); Physica A **249**, 1 (1998).
[5] I.S. Aranson, D. Blair, W. Kwok, G. Karapetrov, U. Welp, G.W. Crabtree, V.M. Vinokur, and L.S. Tsimring, Phys. Rev. Lett. **82**, 731 (1999).
[6] T.H. Metcalf, J.B. Knight, and H.M. Jaeger, Physica A **236**, 202 (1997).
[7] N. Mujica and F. Melo, Phys. Rev. Lett. **80**, 5121 (1998).
[8] C.R. Wassgren, C.E. Brennen, and M.L. Hunt, J. Appl. Mech. **63**, 712 (1996)).
[9] C. Bizon, M.D. Shattuck, J.B. Swift, W.D. McCormick, and H.L. Swinney, Phys. Rev. Lett. **80**, 57 (1998).
[10] J.R. De Bruyn, C. Bizon, M.D. Shattuck, D. Goldman, J.B. Swift, and H.L. Swinney, Phys. Rev. Lett. **81**, 1421 (1998).
[11] S. Luding, E. Clement, J. Rajchenbach, and J. Duran, Europhys. Lett. **36**, 247 (1996).
[12] D. Rothman, Phys. Rev. E **57**, 1239 (1998); E. Cerda, F. Melo, and S. Rica, Phys. Rev. Lett. **79**, 4570 (1997); T. Shinbrot, Nature (London) **389**, 574 (1997); J. Eggers and H. Riecke, Phys. Rev. E **59**, 4476 (1999); S. C. Venkataramani and E. Ott, Phys. Rev. Lett. **80**, 3495 (1998).
[13] C. Crawford and H. Riecke, Physica D **129**, 83 (1999).
[14] L.S. Tsimring and I.S. Aranson, Phys. Rev. Lett. **79**, 213 (1997); I.S. Aranson and L.S. Tsimring, Physica A **249**, 103 (1998).
[15] I.S. Aranson, L.S. Tsimring, and V.M. Vinokur, Phys. Rev. E **59**, 1327 (1999).
[16] P.K. Das and D. Blair, Phys. Lett. A **242**, 326 (1998).
[17] W. Zhang and J. Vinals, Phys. Rev. Lett. **74**, 690 (1995).
[18] S.V. Kiyashko, L.N. Korzinov, M.I. Rabinovich, and L.S. Tsimring, Phys. Rev. E **54**, 5037 (1996).
[19] A. Mehta and J.M. Luck, Phys. Rev. Lett. **65**, 393 (1990).
[20] Note that Eq. (3) also describes the evolution of the order parameter for the parametric instability in vertically oscillating fluids.
[21] M. Cross and P.C. Hohenberg, Rev. Mod. Phys. **65**, 851 (1993).
[22] This analysis is similar to that of Ref. [28], where the stability of hexagons was demonstrated for the SHE. In a certain limit Eq. (3) can be reduced to SHE (see below).
[23] Numerical experiments were performed using the quasispectral split-step method in a 100×100 domain with 256×256 mesh points and periodic boundary conditions.
[24] D.M. Petrich and R.E. Goldstein, Phys. Rev. Lett. **72**, 1120 (1994); R.E. Goldstein, D.J. Muraki, D.M. Petrich, and Phys. Rev. E **53**, 3933 (1996).
[25] The importance of large-scale flow was also indirectly demonstrated in Ref. [10].
[26] P.B. Umbanhowar, Ph. thesis, University of Texas, Austin, 1996.
[27] SHE for oscillatory systems with strong resonance coupling was derived by P. Coullet and K. Emilson, Physica D **61**, 119 (1992).
[28] G. Dewel, S. Métens, M'F. Hilali, P. Borckmans, and C.B. Price, Phys. Rev. Lett. **74**, 4647 (1995).
[29] In Ref. [13] modified Swift-Hohenberg equation was used to describe squares and oscillons.
[30] I. S. Aranson, B. A. Malomed, L. M. Pismen, and L. S. Tsimring (unpublished).
[31] K. Ouchi and H. Fujisaka, Phys. Rev. E **54**, 3895 (1996); K. Staliunas and V.J. Sánchez-Morcillo, Phys. Lett. A **241**, 28 (1998).
[32] H.K. Pak, E. VanDoorn, and R.P. Behringer, Phys. Rev. Lett. **74**, 4643 (1995).
[33] The measured acceleration μ may differ from the applied subharmonic (sinusoidal) driving q since the granular material moves inside the cell. We measure q independently by removing the granular material from the cell.